crystals

MDPI

Article

Dynamic Fracture Mechanism of Quasicrystal-Containing Al–Cr–Fe Consolidated Using Spark Plasma Sintering

Ruitao Li [1,2], Zhiyong Wang [3,*], Zhong Li [4], Khiam Aik Khor [4] and Zhili Dong [2,*]

[1] School of Mechanical Engineering, Jiang Su University, 301 Xuefu Road, Zhenjiang 212013, China; RLI3@e.ntu.edu.sg
[2] School of Materials Science and Engineering, Nanyang Technological University, 50 Nanyang Avenue, Singapore 639798, Singapore
[3] School of Mechatronical Engineering, Beijing Institute of Technology, 5 South Zhongguancun Street, Beijing 100081, China
[4] School of Mechanical and Aerospace Engineering, Nanyang Technological University, 50 Nanyang Avenue, Singapore 639798, Singapore; zli013@e.ntu.edu.sg (Z.L.); mkakhor@ntu.edu.sg (K.A.K.)
* Correspondence: zhiyong_wang@bit.edu.cn (Z.W.); ZLDong@ntu.edu.sg (Z.D.); Tel.: +65-6790 6727 (Z.D.)

Received: 15 August 2018; Accepted: 8 October 2018; Published: 10 October 2018

Abstract: The potential applications of quasicrystals (QCs) in automotive and aerospace industries requires the investigation of their fracture and failure mechanisms under dynamic loading conditions. In this study, Al–Cr–Fe powders were consolidated into pellets using spark plasma sintering at 800 °C for 30 min. The microhardness and dynamic failure properties of the samples were determined using nanoindentation and split-Hopkinson pressure bar technique, respectively. Scanning electron microscopy and transmission electron microscopy were employed to analyze fracture particles. The dynamic failure strength obtained from the tests is 653 ± 40 MPa. The dynamic failure process is dominated by transgranular fracture mechanisms. The difficulty in the metadislocation motion in the dynamic loading leads to the high brittleness of the spark plasma sintered (SPSed) Al–Cr–Fe materials.

Keywords: quasicrystals; spark plasma sintering; microstructures; fracture; transmission electron microscopy

---

1. Introduction

Quasicrystals (QCs) provide high hardness, high wear resistance, low thermal conductivity, good corrosion resistance, good oxidation resistance and hydrogen storage capability due to their unique atomic arrangement [1–5]. It is widely discussed that QCs can be applied as reinforcements in composites and protective coatings [6–8]. The materials containing QCs can be potentially used in automotive and aerospace sectors where the impact properties of materials are of great importance [2,6]. The mechanical behavior of QCs at high strain rates is a key consideration in the design and optimization of composites reinforced with them. Thus, the understanding of the failure and deformation mechanisms of QCs under dynamic strain rates and stress states is vital for the development of composites reinforced with them.

Al–Cr–Fe is among several commercially available quasicrystal powders. In the Al rich corner, the Al–Cr–Fe system is known to contain quasicrystals (icosahedral and decagonal phases) and their approximants (rhombohedral, orthorhombic, cubic and hexagonal phases) [9–12]. Due to the high Cr element, this alloy exhibits good corrosion resistance and oxidation resistance [13]. In addition, it also has unique optical properties because of its special atomic arrangement [14]. To expand its potential applications, quasicrystal-containing Al–Cr–Fe alloy is commercially produced in the form of powders with spherical shape and good flowability [15]. To further investigate its properties, including dynamic properties, it is necessary to consolidate the powders into bulk materials first. Among the various consolidation techniques for QCs is spark plasma sintering (SPS). In the SPS process, pulsed current and pressure play their roles simultaneously: the pressure can cause plastic flow of powders, especially at high temperatures; the current can promote diffusion of atoms, hence facilitating the sintering [16,17]. Therefore, SPS is an appropriate method for consolidating Al–Cr–Fe powders.

Most of the studies on QCs focus on the quasicrystalline structure and physical properties [18–22]. For some stable QCs with a polycrystalline structure, obvious temperature-induced influences on hardness and thermal expansion have been observed [23–25]. In addition, studies on the equilibrium phase diagram, the effect of annealing on the quality of the stable icosahedral structure, and the orientation dependence on icosahedral phase growth have been conducted [25–28]. However, the mechanical properties of QCs at dynamic deformation rates are seldom reported. Because of their potential application in high speed areas, the accurate characterization of the dynamic behavior of QCs materials is necessary to predict their service performance. Typically, the dynamic behavior of materials can be characterized using a split-Hopkinson pressure bar (SHPB) technique [29–31]. It is expected that this technique can be applied to characterize the dynamic performance of QCs despite their relatively low failure strain [30,32].

The aim of this study is to investigate the dynamic fracture mechanism of QCs subjected to dynamic loads. Al–Cr–Fe powders were first consolidated into dense pellets using SPS. Dynamic uniaxial experiments in a SHPB system were subsequently performed to investigate the dynamic deformation and fracture mechanisms of the SPSed pellets. The fracture surfaces on Al–Cr–Fe QC fragments were examined using scanning electron microscopy (SEM) and transmission electron microscopy (TEM) to further explore the fracture mechanisms during dynamic deformation.

2. Materials and Methods

2.1. Sample Preparation

The $Al_{70}Cr_{20}Fe_{10}$ powders were purchased from Saint Gobian, Courbevoie, France. They were consolidated using SPS apparatus (Sumitomo Coal Mining Company Ltd., Tokyo, Japan) in a graphite mold at 800 °C for 30 min in vacuum (<10 Pa). One gram of Al–Cr–Fe powders was loaded into a graphite mold with an inner diameter of 10 mm. The sintering was conducted with a constant heating and cooling rate of 100 °C/min with an applied pressure of 50 MPa. Cylindrical samples of 10 mm in diameter and 3 mm in length were prepared for the investigation of the mechanical properties at dynamic strain rates.

2.2. Nanoindentation Tests

The microhardness of the pellets was determined using CSM microhardness tester (Laboratory Testing Inc. Philadelphia, PA, USA). The load was 9.8 N and the holding time 10 s. Sixteen random points were chosen for the test. Mechanical properties of the pellets were also evaluated from the load–displacement curves obtained from nanoindentation tests using Agilent G200 Nanoindenter (Keysight Technologies, Santa Rosa, CA, USA) with a Berkovich diamond indenter. The indentation was performed in the depth-control mode with an indentation depth of 128 nm. The elastic modulus and hardness are directly obtained from the indentation force and the penetration depth measurements of indenter of known properties and shape.

2.3. Split-Hopkinson Pressure Bar Experiments

The dynamic uniaxial compressive tests of Al–Cr–Fe samples were performed in a conventional SHPB system, as schematically shown in Figure 1. The test system consisted of projectile, input and output bars with the length of 300, 1000 and 1000 mm, respectively. The bars were all made of YAG300 maraging steel with a diameter D_0 = 12.7 mm, Young's modulus E_0 = 197 GPa, density

$\rho_0 = 7766.5$ kg/m^3 and Poisson's ratio $\nu_0 = 0.3$. In the SHPB test, an elastic compressive incident pulse ε_i was generated by the impact of the projectile onto the input bar. When this incident wave propagated to the bar-specimen interface, part of the wave ε_r was reflected back into the input bar, and the remaining portion ε_t was transmitted into the output bar through the specimen. The strain gauges mounted on the bars measured the stress/strain waves propagating in these bars, from which the stress and strain histories can be determined with the assumption of axial uniformity of specimen stress and strain fields. The subsequent analysis of measured stress/strain waves was detailed in our previous work [30], including the noise reduction, wave dispersion correction, alignment of the measured waves to the bar-specimen interfaces, and the verification of the force equilibrium at the specimen ends. Finally, the dynamic mechanical properties of the sintered Al–Cr–Fe material can be determined based on the calculated stress and strain histories. Note that the specimen ends were all well lubricated with Castrol LMX grease to minimize the interfacial frictional effect in all the dynamic tests [33].

2.4. Microstructural Characterization

To further explore the fracture mechanisms, specimen fragments were carefully collected after each dynamic test. Both scanning electron microscope (FESEM, JEOL 7600, JEOL, Tokyo, Japan) and high-resolution transmission electron microscope (TEM, JEOL 2100F, JEOL, Tokyo, Japan) were used to characterize their microstructure. To prepare the TEM samples of Al–Cr–Fe powders, as-received powders and epoxy were first blended and then cured to form a bulk compact epoxy-powder composite. Subsequently, the composite mixture was sawed, mechanically polished, dimpled and finally ion-milled to get electron-transparent TEM samples. The TEM samples of sintered Al–Cr–Fe pellets was prepared by conventional mechanical polishing, dimpling and ion-milling. The TEM sample of fragments was prepared by dispersing them in alcohol and then dropping the suspension onto a carbon-coated copper grid for air drying. The smaller fragments after dynamic tests were found to have very thin edges that are electron-transparent and ideal for TEM observation.

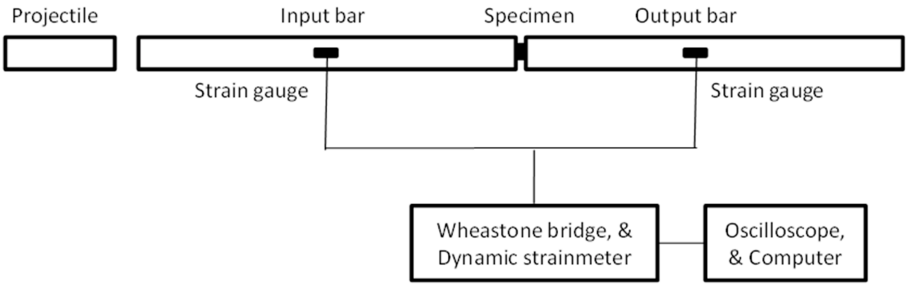

Figure 1. The schematic of the split-Hopkinson pressure bar system.

3. Results

3.1. Microstructure

Figure 2a shows a typical bright field TEM image of as-received Al–Cr–Fe powders. It can be observed that the grains are in micro to sub-micro scale with dendritic structure and that high-density planar faults are present, as indicated by the red arrows. These planar faults are related to a unique defect in the quasicrystal approximants: metadislocation. In this type of defect, a dislocation core is connected to several phason planes, meditating the plastic deformation of these materials [34]. Figure 2b shows a dark field TEM image of the SPSed Al–Cr–Fe. It can be found that the grains become polygonal. The variation of grain morphology before and after the sintering indicates that the grains have grown in the sintering process. In addition, high-density of striped planar faults can also be observed in the grains of the consolidated pellets (indicated by the blue arrows in Figure 2b). This indicates the planar faults are easy to form in this alloy, in both gas atomization process and the later sintering process. However, the specific formation mechanism of these planar faults still needs to be further investigated. The SAED patterns (Figure 2c,d) verify the existence of both icosahedral (I-AlCrFe) and decagonal (D-AlCrFe) phases in the SPSed pellets. Two of their approximants, rhombohedral $Al_8(Cr,Fe)_5$ and cubic-brass $Al_9(Cr,Fe)_4$, are also present. The Al–Cr–Fe powders and sintering process in this study were the same as in our previous experiments [35], so the composition of phases in the powders and SPSed samples was identical in these experiments. The detailed crystallographic and compositional information of the as-received powders and SPSed pellets can be found in our previous report [35]—note that the samples in this study are dense.

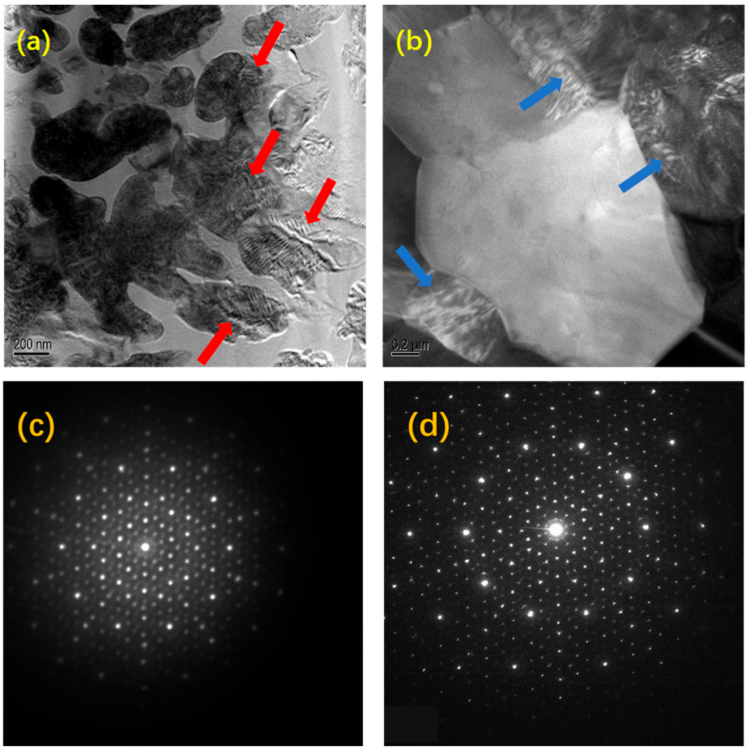

Figure 2. TEM study of as-received Al–Cr–Fe powders and as-sintered Al–Cr–Fe pellets: (**a**) bright field TEM image of as-received Al–Cr–Fe powder; (**b**) dark field TEM image of as-SPSed Al–Cr–Fe (the arrows in both images indicate planar faults); (**c**) SAED pattern taken along the 5-fold axis of icosahedral phase; and (**d**) SAED pattern taken along the 10-fold axis of decagonal phase.

3.2. Microhardness and Young's Modulus

The microhardness measured by CSM microhardness tester is Hv 810, which is close to the reported values of annealed $Al_{65}Cu_{20}Fe_{15}$ QC (Hv 844) and $Al_{64}Cu_{22.5}Fe_{13.5}$ QC (Hv 804) [36]. Microhardness, together with elastic modulus, is also provided by nanoindentation tests. Figure 3 shows the representative load–displacement curves obtained from the nanoindentation tests in different positions of a sample. The values of elastic modulus and hardness can be calculated by measuring the slope of the unloading portion and the penetration depth, respectively. The measured Young's modulus and microhardness are 199.7 ± 5.3 GPa and 13.3 ± 0.4 GPa, respectively. The measured Young's modulus is close to the reported value of $Al_{70}Pd_{20}Mn_{10}$ QC [37].

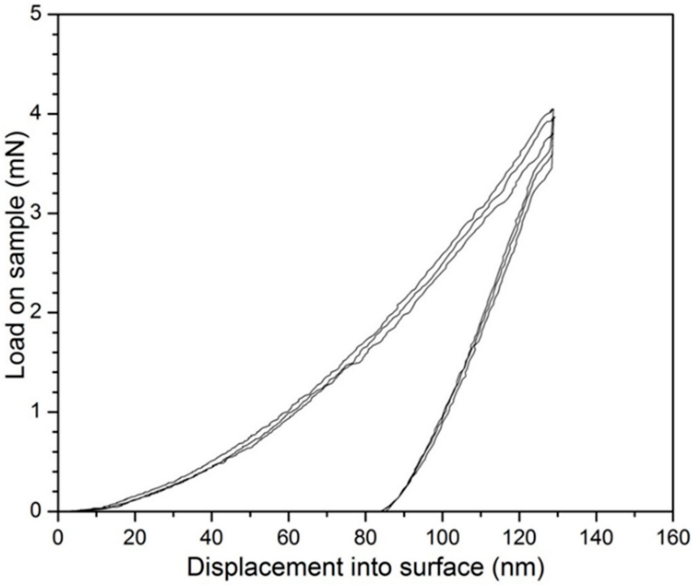

Figure 3. Nanoindentation curves obtained from different regions of Al–Cr–Fe.

3.3. Dynamic Mechanical Response

Figure 4 shows the alignment of the measured strain wave signals after noise reduction and wave dispersion correction to the bar-specimen interfaces. The transmitted strain wave (ε_t) signal was compared to the sum of incident (ε_i) and reflected (ε_r) strain wave signals to verify the assumption of homogeneous deformation and one-dimensional elastic wave propagation. To quantify the force equilibrium, a coefficient η was defined by the following equation [38].

$$\eta = 2\left|\frac{F_{in} - F_{out}}{F_{in} + F_{out}}\right| = 2\left|\frac{\varepsilon_i + \varepsilon_r - \varepsilon_t}{\varepsilon_i + \varepsilon_r + \varepsilon_t}\right| \tag{1}$$

where F_{in} and F_{out} represent the forces at specimen ends next to input and output bars, respectively.

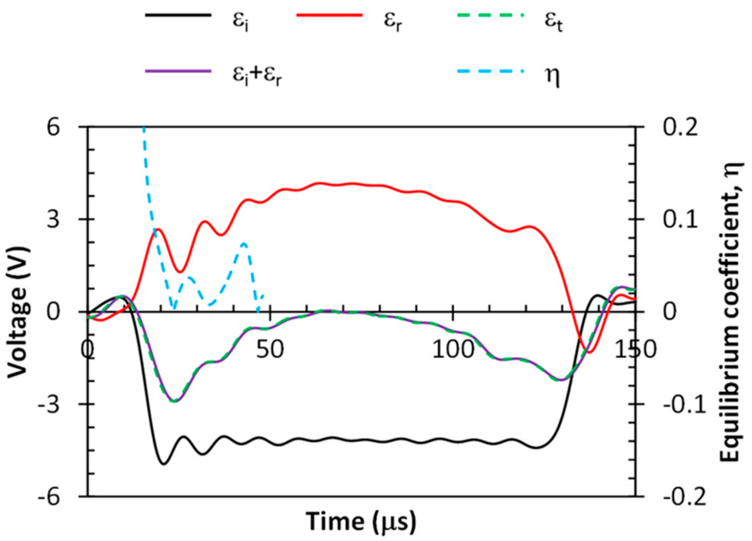

Figure 4. Verification of force equilibrium at specimen ends in the SHPB test of an Al–Cr–Fe specimen.

In Figure 4, the forces at specimen ends are not in equilibrium ($\eta > 5\%$) at the very beginning of the loading during the SHPB compression. With the increase of the loading, the coefficient η reduces to less than 5% quickly, indicating that force equilibrium is reached [38]. Therefore, the assumption of axial stress uniformity has been verified. Subsequently, the stress and strain histories can be determined by Equations (2) and (3):

$$\sigma(t) = \frac{A_0 E_0}{A} \varepsilon_t(t) \tag{2}$$

$$\varepsilon(t) = \frac{2c_0}{l} \int_0^t [\varepsilon_i(\tau) - \varepsilon_t(\tau)] d\tau \tag{3}$$

where l is the length of specimen; A_0 and A are the cross-sectional areas of the bars and specimen, respectively; and t is time.

The representative stress–strain responses at a strain rate of ~800° s^{-1} can be found in Figure 5. Previous research has found that there is a critical value of strain rate, above which materials demonstrate a rate dependent feature [30,31,39]. As the strain rate increases from zero to the designed dynamic level in the SHPB test, the elastic modulus can be considered to be insensitive to the strain rate at the beginning of the loading stage [30,31]. The elastic modulus can be determined by the slope of the initial linear portion of the stress–strain curves. The measured value, 197.1 ± 0.6 GPa, is quite close to the one obtained from the nanoindentation tests. This consistency further indicates that the SPSed Al–Cr–Fe materials are fully dense with few micropores. In addition, the dynamic failure strength obtained from the tests is 653 ± 40 MPa.

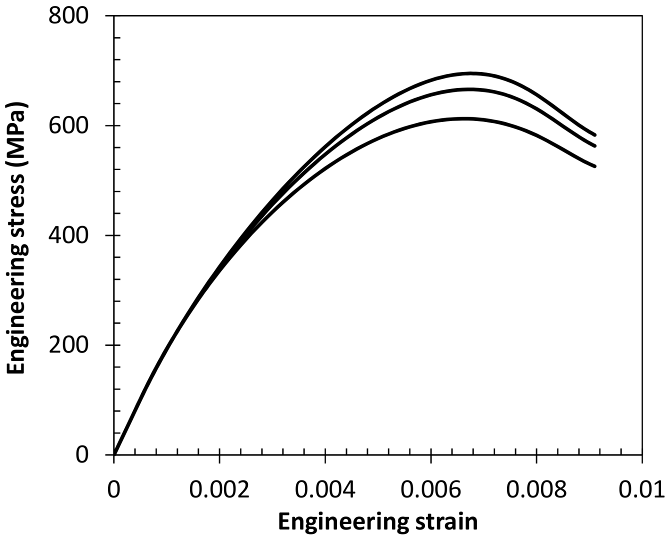

Figure 5. Stress–strain curves at dynamic strain rate of ~800 s^{-1}.

4. Discussion

It is well known that QCs demonstrate brittle nature at quasi-static strain rates at room temperature [40,41]. In Figure 5, only elastic deformation happens at the very early stage of the SHPB compression, where the forces at specimen ends are inequilibrium (η > 5%, refer to Figure 4). With the increase of the load to its maximum, specimen deforms inelastically, implying that it is high likely that the impact energy is dissipated during dynamic loads. Meanwhile, a decrease of the slope of the stress–strain curves represents the occurrence of material degradation during dynamic compression, which might be caused by a few stress concentration-induced micro-cracks at the circumferential edges of the specimen ends due to the friction-induced multiaxial stress states [31]. After the peak stress is reached, the significant drop of the stress reveals the catastrophic failure of the SPSed Al–Cr–Fe materials due to fast propagation of a large number of cracks in the specimen.

The failure paths and fracture mechanisms during dynamic compression tests were investigated by SEM and TEM observation of the fragments collected after the dynamic experiments. Figure 6 exhibits a typical fracture surface. This surface is flat with some cleavage steps on it, indicating that the cracks proceed with small deflections in some regions. In addition, the stepped micro-fracture (indicated by the black arrow) seems to be the slip bands. However, cracks propagate primarily in a transgranular mode.

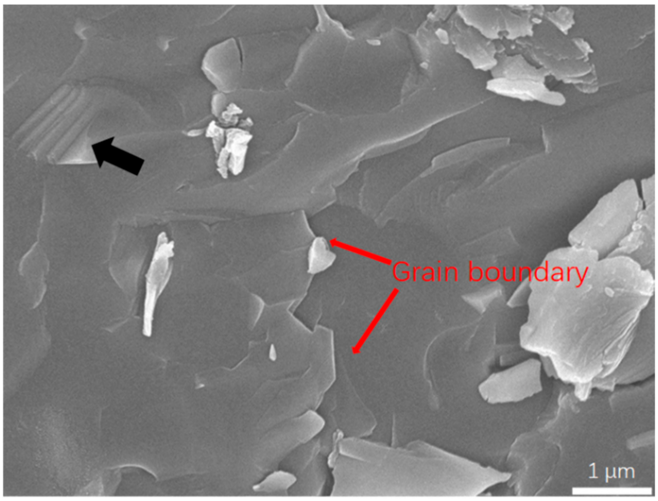

Figure 6. Fracture surface of the SPSed Al–Cr–Fe pellets.

Figure 7 shows a bright field TEM image of a fragment with a micro-crack. The microcrack runs through a grain. Moreover, the crack is straight with small deflections at some locations. This further proves that the failure process of this material is mainly governed by transgranular fracture mechanism in the dynamic compressive tests.

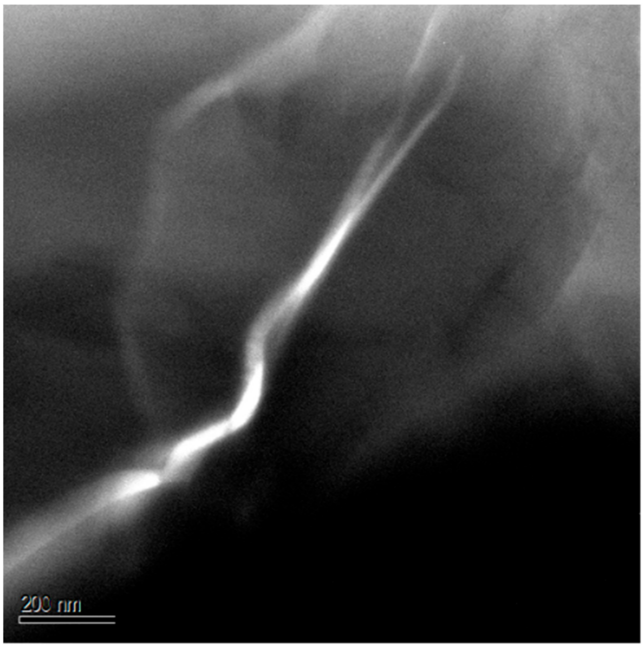

Figure 7. Bright field TEM image of a fragment with crack.

It is interesting to note that the edges of the fragments are featured with high density of planar faults, as illustrated in Figure 8a,b. The HRTEM image (Figure 8c) also shows that there exists an evident disorder of atomic arrangement in the region. Generally, these characteristics indicate high plasticity. Nevertheless, the SPSed samples exhibited little plasticity in the experiments. This is due to the complex atomic arrangement in them. The plastic deformation of QCs and their approximants involves metadislocation formation and motion, which require the local atomic jump of thousands of atoms; only at high temperatures is diffusive motion greatly facilitated and thus metadislocation motion activated. Therefore, these materials cannot deform at room temperature due to the difficulty of metadislocation motion. That is, the planar faults were not formed as a consequence of the impact at room temperature.

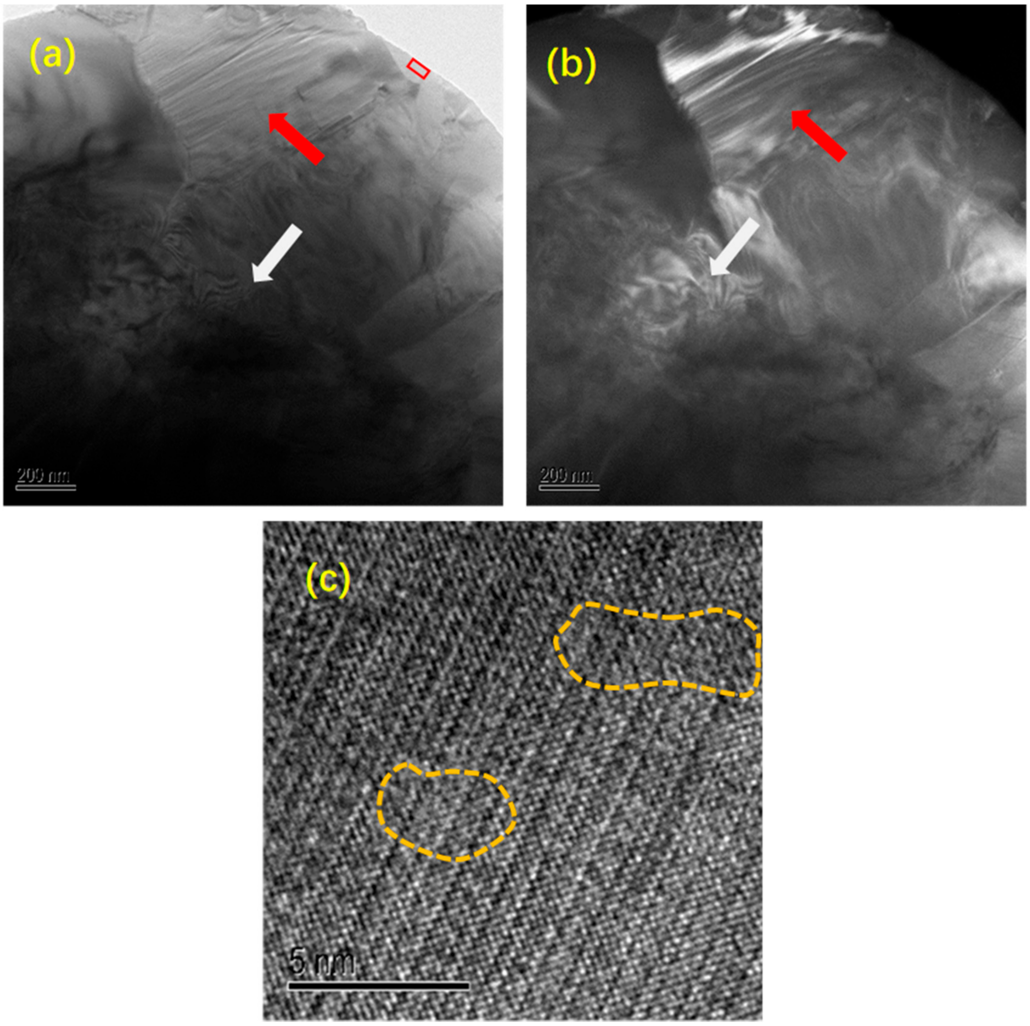

Figure 8. (**a**) Bright and (**b**) dark-field TEM images of a fragment edge after the dynamic compression test; and (**c**) HR-TEM image of the boxed area in (**a**).

5. Conclusions

The dynamic behavior of the SPSed Al–Cr–Fe was investigated in SHPB experiments for the first time. Both SEM and TEM were employed to examine the fracture surfaces of the fragments to explore the fracture mechanism. The conclusions were drawn as follows:

The dynamic mechanical responses of the SPSed Al–Cr–Fe has been experimentally determined in a SHPB test with the verification of the assumption of homogeneous deformation and one-dimensional elastic wave propagation to support the reliable calculation of stress and strain histories, especially for the material with brittle nature (quite small failure strain).

The initial elastic modulus for the dynamic stress–strain response is insignificantly dependent upon strain rates. The consistency between the dynamic test and nanoindentation measurement indicates that the Al–Cr–Fe powders are fully consolidated.

The dynamic failure process subjected to uniaxial compressive loads is dominated by transgranular fracture mechanisms, although the deflection of cracking paths occurs in some regions. The difficulty of metadislocation motion at low temperatures leads to the high brittleness of Al–Cr–Fe.

Author Contributions: Conceptualization, Z.D. and R.L.; Methodology, R.L. and Z.W.; Validation, Z.D.; Formal Analysis, R.L., Z.W., and Z.L.; Investigation, R.L., Z.W. and Z.L.; Data Curation, Z.W.; Writing—Original Draft Preparation, R.L. and Z.W.; Writing—Review and Editing, Z.D. and K.A.K.; Supervision, Z.D.; Project Administration, Z.D. and K.A.K.; and Funding Acquisition, Z.D.

Funding: This research was funded by the Ministry of Education, Singapore, grant number RG93/16.

Acknowledgments: The electron microscopy was performed at the Facility for Analysis, Characterization, Testing and Simulation (FACTS) in Nanyang Technological University, Singapore.

Conflicts of Interest: The authors declare no conflict of interest.

References

1. Wolf, B.; Bambauer, K.-O.; Paufler, P. On the temperature dependence of the hardness of quasicrystals. *Mater. Sci. Eng. A* **2001**, *298*, 284–295. [CrossRef]
2. Dubois, J.-M. New prospects from potential applications of quasicrystalline materials. *Mater. Sci. Eng. A* **2000**, *294*, 4–9. [CrossRef]
3. Fu, Y.; Kang, N.; Liao, H.; Gao, Y.; Coddet, C. An investigation on selective laser melting of Al-Cu-Fe-Cr quasicrystal: From single layer to multilayers. *Intermetallics* **2017**, *86*, 51–58. [CrossRef]
4. Zhao, J.; Zhai, X.; Tao, X.; Li, Z.; Wang, Q.; Liu, W.; Wang, L. Improved electrochemical hydrogen storage capacity of $Ti_{45}Zr_{38}Ni_{17}$ quasicrystal by addition of ZrH_2. *J. Mater. Sci. Technol.* **2017**, *34*, 995–998. [CrossRef]
5. Li, R.; Murugan, V.K.; Dong, Z.; Khor, K.A. Comparative Study on the Corrosion Resistance of Al–Cr–Fe Alloy Containing Quasicrystals and Pure Al. *J. Mater. Sci. Technol.* **2016**, *32*, 1054–1058. [CrossRef]
6. Dubois, J.-M. Properties-and applications of quasicrystals and complex metallic alloys. *Chem. Soc. Rev.* **2012**, *41*, 6760–6777. [CrossRef] [PubMed]
7. Ali, F.; Scudino, S.; Anwar, M.; Shahid, R.; Srivastava, V.; Uhlenwinkel, V.; Stoica, M.; Vaughan, G.; Eckert, J. Al-based metal matrix composites reinforced with Al–Cu–Fe quasicrystalline particles: Strengthening by interfacial reaction. *J. Alloy. Compd.* **2014**, *607*, 274–279. [CrossRef]
8. Li, R.; Dong, Z.; Khun, N.W.; Khor, K.A. Novel Ti based metal matrix composites reinforced with Al–Cr–Fe quasicrystals approximants. *Mater. Sci. Technol.* **2015**, *31*, 688–694. [CrossRef]
9. Demange, V.; Machizaud, F.; Dubois, J.M.; Anderegg, J.W.; Thiel, P.A.; Sordelet, D.J. New approximants in the Al–Cr–Fe system and their oxidation resistance. *J. Alloy. Compd.* **2002**, *342*, 24–29. [CrossRef]
10. Pavlyuchkov, D.; Balanetskyy, S.; Kowalski, W.; Surowiec, M.; Grushko, B. Stable decagonal quasicrystals in the Al-Fe-Cr and Al-Fe-Mn alloy systems. *J. Alloy. Compd.* **2009**, *477*, L41–L44. [CrossRef]
11. Demange, V.; Ghanbaja, J.; Beeli, C.; Machizaud, F.; Dubois, J.M. Study of decagonal approximant and γ-brass-type compounds in Al Cr Fe thin films. *J. Mater. Res.* **2004**, *19*, 2285–2297. [CrossRef]
12. Palm, M. The Al–Cr–Fe system–Phases and phase equilibria in the Al-rich corner. *J. Alloy. Compd.* **1997**, *252*, 192–200. [CrossRef]
13. Demange, V.; Anderegg, J.W.; Ghanbaja, J.; Machizaud, F.; Sordelet, D.J.; Besser, M.; Thiel, P.A.; Dubois, J.M. Surface oxidation of Al–Cr–Fe alloys characterized by X-ray photoelectron spectroscopy. *Appl. Surf. Sci.* **2001**, *173*, 327–338. [CrossRef]
14. Demange, V.; Milandri, A.; De Weerd, M.C.; Machizaud, F.; Jeandel, G.; Dubois, J.M. Optical conductivity of Al-Cr-Fe approximant compounds. *Phys. Rev. B* **2002**, *65*, 144205. [CrossRef]
15. Shaĭtura, D.; Enaleeva, A. Fabrication of quasicrystalline coatings: A review. *Crystallogr. Rep.* **2007**, *52*, 945–952. [CrossRef]
16. Li, R.; Dong, Z.; Khor, K.A. Spark plasma sintering of Al–Cr–Fe quasicrystals: Electric field effects and densification mechanism. *Scr. Mater.* **2016**, *114*, 88–92. [CrossRef]
17. Gendre, M.; Maitre, A.; Trolliard, G. A study of the densification mechanisms during spark plasma sintering of zirconium (oxy-) carbide powders. *Acta Mater.* **2010**, *58*, 2598–2609. [CrossRef]
18. Zheng, J.-C.; Huan, C.; Wee, A.; Van Hove, M.A.; Fadley, C.S.; Shi, F.; Rotenberg, E.; Barman, S.R.; Paggel, J.J.; Horn, K. Atomic-scale structure of the fivefold surface of an AlPdMn quasicrystal: A quantitative x-ray photoelectron diffraction analysis. *Phys. Rev. B* **2004**, *69*, 134107. [CrossRef]
19. Shulyatev, D.; Klyueva, M.; Devaradjan, U. Anisotropy of the electric transport properties of decagonal Al–Cu–Co (Fe) quasicrystals. *Phys. Met. Metallogr.* **2016**, *117*, 883–888. [CrossRef]

20. Suck, J.-B.; Schreiber, M.; Häussler, P. *Quasicrystals: An Introduction to Structure, Physical Properties and Applications*; Springer Science & Business Media: Berlin, Germany, 2013.
21. Chen, Y.; Qiang, J.; Dong, C. Smearing-type wear behavior of $Al_{62}Cu_{25.5}Fe_{12.5}$ quasicrystal abrasive on soft metals. *Intermetallics* **2016**, *68*, 23–30. [CrossRef]
22. Laplanche, G.; Bonneville, J.; Joulain, A.; Gauthier-Brunet, V.; Dubois, S. Mechanical properties of Al–Cu–Fe quasicrystalline and crystalline phases: An analogy. *Intermetallics* **2014**, *50*, 54–58. [CrossRef]
23. Mordyuk, B.; Prokopenko, G.; Milman, Y.V.; Iefimov, M.; Grinkevych, K.; Sameljuk, A.; Tkachenko, I. Wear assessment of composite surface layers in Al–6Mg alloy reinforced with AlCuFe quasicrystalline particles: Effects of particle size, microstructure and hardness. *Wear* **2014**, *319*, 84–95. [CrossRef]
24. Watanuki, T.; Kashimoto, S.; Ishimasa, T.; Machida, A.; Yamamoto, S.; Tanaka, Y.; Mizumaki, M.; Kawamura, N.; Watanabe, S. Thermal expansion of a Au–Al–Yb intermediate valence quasicrystal. *Solid State Commun.* **2015**, *211*, 19–22. [CrossRef]
25. Tsai, A.P.; Suenaga, H.; Ohmori, M.; Yokoyama, Y.; Inoue, A.; Masumoto, T. Temperature dependence of hardness and expansion in an icosahedral Al-Pd-Mn alloy. *Jpn. J. Appl. Phys.* **1992**, *31*, 2530–2531. [CrossRef]
26. Yokoyama, Y.; Tsai, A.-P.; Inoue, A.; Masumoto, T. Production of Quasicrystalline Al–Pd–Mn Alloys with Large Single Domain Size. *Mater. Trans. JIM* **1991**, *32*, 1089–1097. [CrossRef]
27. Louzguine-Luzgin, D.; Inoue, A. Formation and properties of quasicrystals. *Annu. Rev. Mater. Res.* **2008**, *38*, 403–423. [CrossRef]
28. Kang, H.; Li, X.; Wang, T.; Liu, D.; Su, Y.; Hu, Z.; Guo, J.; Fu, H. Crystal–quasicrystal transition depending on cooling rates in directionally solidified Al–3Mn–7Be (at.%) alloy. *Intermetallics* **2014**, *44*, 101–105. [CrossRef]
29. Li, P.; Wang, Z. Experimental Characterization and Modified Constitutive Modeling of the Strain Rate Dependent Compressive Behavior of Adhesives. *Macromol. Mater. Eng.* **2016**, *301*, 577–585. [CrossRef]
30. Wang, Z.; Li, P. Characterisation of dynamic behaviour of alumina ceramics: Evaluation of stress uniformity. *AIP Adv.* **2015**, *5*, 107224. [CrossRef]
31. Wang, Z.; Li, P. Dynamic failure and fracture mechanism in alumina ceramics: Experimental observations and finite element modelling. *Ceram. Int.* **2015**, *41*, 12763–12772. [CrossRef]
32. Forrestal, M.; Wright, T.; Chen, W. The effect of radial inertia on brittle samples during the split Hopkinson pressure bar test. *Int. J. Impact. Eng.* **2007**, *34*, 405–411. [CrossRef]
33. Li, P.; Siviour, C.; Petrinic, N. The effect of strain rate, specimen geometry and lubrication on responses of aluminium AA2024 in uniaxial compression experiments. *Exp. Mech.* **2009**, *49*, 587–593. [CrossRef]
34. Klein, H.; Feuerbacher, M.; Schall, P.; Urban, K. Novel Type of Dislocation in an Al-Pd-Mn Quasicrystal Approximant. *Phys. Rev. Lett.* **1999**, *82*, 3468–3471. [CrossRef]
35. Li, R.; Dong, Z.; Murugan, V.K.; Zhang, Z.; Khor, K.A. Microstructure characterization of Al–Cr–Fe quasicrystals sintered using spark plasma sintering. *Mater. Charact.* **2015**, *110*, 264–271. [CrossRef]
36. Suárez, M.; Esquivel, R.; Alcántara, J.; Dorantes, H.; Chávez, J. Effect of chemical composition on the microstructure and hardness of Al–Cu–Fe alloy. *Mater. Charact.* **2011**, *62*, 917–923. [CrossRef]
37. Yokoyama, Y.; Inoue, A.; Masumoto, T. Mechanical properties, fracture mode and deformation behavior of Al70Pd20Mn10 single-quasicrystal. *Mater. Trans. JIM* **1993**, *34*, 135–145. [CrossRef]
38. Zhu, J.; Hu, S.; Wang, L. An analysis of stress uniformity for concrete-like specimens during SHPB tests. *Int. J. Impact. Eng.* **2009**, *36*, 61–72. [CrossRef]
39. Subhash, G.; Ravichandran, G. Mechanical behaviour of a hot pressed aluminum nitride under uniaxial compression. *J. Mater. Sci.* **1998**, *33*, 1933–1939. [CrossRef]
40. Takeuchi, S.; Iwanaga, H.; Shibuya, T. Hardness of quasicrystals. *Jpn. J. Appl. Phys.* **1991**, *30*, 561–562. [CrossRef]
41. Mikulla, R.; Stadler, J.; Krul, F.; Trebin, H.-R.; Gumbsch, P. Crack propagation in quasicrystals. *Phys. Rev. Lett.* **1998**, *81*, 3163–3166. [CrossRef]